

NO-A191 743

AXISYMMETRIC VISCID-INVISCID INTERACTION BY A FROZEN
VORTICITY APPROXIMAT. (U) PENNSYLVANIA STATE UNIV
UNIVERSITY PARK APPLIED RESEARCH LAB. G H HOFFMAN

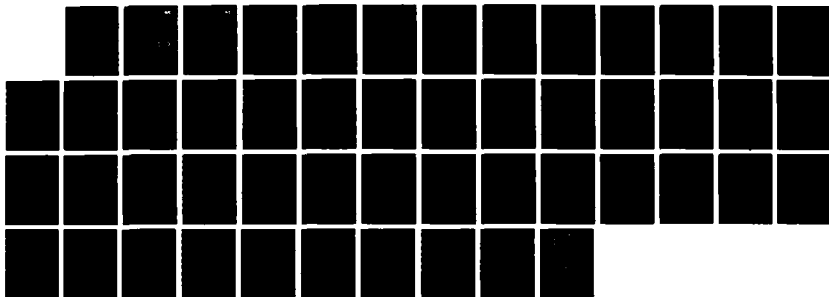
1/1

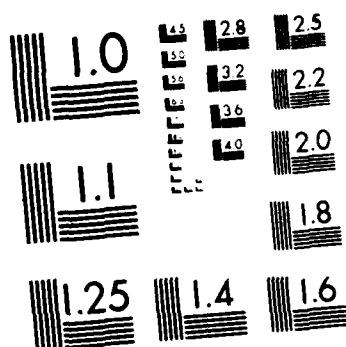
UNCLASSIFIED

14 JAN 88 TH-88-12 N00014-85-C-6041

F/G 20/4

NL





Applied Research Laboratory
The Pennsylvania State University
Post Office Box 30
State College, PA 16804



AD-A191 743

AXISYMMETRIC VISCID-INVISCID INTERACTION BY
A FROZEN VORTICITY APPROXIMATION

G. H. Hoffman

Technical Memorandum
File No. TM 88-12
14 January 1988
Contract No. N00024-85-C-6041

Copy No. 1

DTIC
ELECTE
FEB 12 1988
S & H D

Approved for Public Release
Distribution Unlimited

Department of the Navy
Space and Naval Warfare Systems Command
Contract No. N00024-85-C-6041

88 2 09 050

Applied Research Laboratory
The Pennsylvania State University
Post Office Box 30
State College, PA 16804



AXISYMMETRIC VISCID-INVISCID INTERACTION BY
A FROZEN VORTICITY APPROXIMATION

G. H. Hoffman

Technical Memorandum
File No. TM 88-12
14 January 1988
Contract No. N00024-85-C-6041

Copy No. _____

Approved for Public Release
Distribution Unlimited

Accession For	
NTIS GRA&I	<input checked="" type="checkbox"/>
DTIC TAB	<input type="checkbox"/>
Unannounced	<input type="checkbox"/>
Justification	
By _____	
Distribution/ _____	
Availability Codes	
Dist	Avail and/or Special
A-1	



Department of the Navy
Space and Naval Warfare Systems Command
Contract No. N00024-85-C-6041

From: G. H. Hoffman

Subject: Axisymmetric Viscid-Inviscid Interaction by a Frozen Vorticity Approximation

References: See Page 33

Abstract: A numerical solution procedure capable of a high degree of automation is presented for calculating the flow field associated with viscid-inviscid interaction on a body of revolution. The method makes use of ideas from asymptotic triple deck analysis of the trailing edge problem. A simpler problem is solved in which two layers are postulated, an outer inviscid, rotational layer (frozen vorticity) which largely governs the pressure in the trailing edge region, and an inner turbulent layer which is modeled in a simple manner. These two layers are patched at a fixed distance from the wall and wake centerline rather than asymptotically matched. The method allows the viscid-inviscid interaction solution to be computed in four iterations, none of which require any user intervention. A high degree of automation is achieved in the computer code because of three factors: (1) the solution cycle is very stable, (2) all calculations use a common streamwise grid, and (3) information is transferred to successive stages of the calculation by computer generated files. Numerical solutions are presented for three bodies and the results compared with published experimental data.

Introduction

The standard approach for solving the axisymmetric viscid-inviscid interaction problem is the displacement body method of which numerous examples have appeared in the literature [1-3]. In this procedure the boundary-layer displacement thickness is added to the body to obtain an approximation to the strong interaction pressure distribution. Since the displacement thickness depends on knowing the pressure distribution, iteration is required to find the solution. In the direct mode (pressure distribution given) the boundary-layer solution invariably produces a displacement thickness which has numerical noise in the strong interaction region. This "noise" is then amplified into pressure wiggles in the potential flow solution. To obtain convergence, numerical smoothing of the pressure distribution is required between each iteration. This process requires intervention by the user and is thus difficult to automate. A variation of the displacement body method is to solve the boundary-layer portion in the inverse mode which results in a numerical smoothing effect. An example of this approach is the work of Carter and Wornom [4].

A promising alternative approach for the solution of the axisymmetric viscid-inviscid interaction problem is to adopt the main ideas of asymptotic analysis as applied to the two-dimensional trailing edge problem. This approach has a firm foundation mathematically and, as it turns out, can be readily automated.

The turbulent flow near a 2-D trailing edge was first analyzed using asymptotic methods by Melnick, Chow and Mead [5] who found that a three-

layer structure develops which extends over a streamwise distance of the order of $(1/\ln Re)$. In the outer layer, because of the small streamwise length scale, viscous terms can be neglected leaving only the inertial terms. Thus the flow in this layer is inviscid but rotational, the vorticity arising from the upstream boundary layer. An inner viscous layer is required to satisfy the no-slip condition and an intermediate, or blending, layer accounts for the different rates of growth of the inner and outer layers. Although the extent of the streamwise effect may differ, the same type of three-layer structure arises in the vicinity of an axisymmetric trailing edge.

Analytical solutions of the 2-D turbulent trailing edge using the three-layer asymptotic approach have been obtained by Melnick, Chow and Mead for a cusped trailing edge and by Melnick and Grossman [6] for a small but nonzero trailing edge angle. These solutions clearly demonstrate the importance of normal pressure gradient (via the outer rotational inviscid layer) in the correct description of the flow at the trailing edge.

Prior to the work of Melnick et al., the only other analytical treatment of the 2-D turbulent trailing edge was by Kuchemann [7]. He considered a wedge-shaped trailing edge of finite angle in the presence of rotational, inviscid flow with constant vorticity. Since the inner layers were neglected, a slip velocity at the wall was required to avoid a constant pressure on the wedge surface. His main finding was that the velocity field induced by the vorticity in the wake retarded the flow on the wedge upstream of the trailing edge which led to separation if the wedge angle was large enough.

In the axisymmetric case, Geller [8] and Hoffman [9] have made use of an outer rotational, inviscid layer to determine flow near the trailing edge. In Geller's procedure a local body oriented Cartesian coordinate system is used and $\partial v / \partial x$ is neglected in the vorticity. As a result, the velocity profile at a given body station is obtained by solving an ordinary differential equation rather than an elliptic partial differential equation, as is ordinarily the case. He patches the inviscid, rotational profile at a given normal distance from the body surface with a one-seventh power law turbulent boundary-layer representation in the inner region. Agreement of calculated velocity profiles near the trailing edge with experimental data is very good. He also finds that the computed velocity profile in the outer region is not sensitive to the assumed profile in the inner region. Hoffman solves the elliptic problem in terms of the stream function. His solution, which neglects patching with the inner layer, allows for velocity slip at the wall, as in the 2-D treatment by Kuchemann. As a result of this neglect, he finds the solution to be fairly sensitive to choice of the initial station where the rotational calculation begins.

In the present work the findings of 2-D asymptotic analysis are applied in an approximate fashion to the axisymmetric trailing edge. Instead of a full triple deck treatment, only the outer layer is solved exactly, the intermediate layer is neglected and the inner layer is modeled in a simple manner. This work, therefore, represents an extension of Reference 9.

Since asymptotic matching is inappropriate in the present scheme, the inner and outer layers are "patched" at a small, fixed distance from

the body surface and wake centerline. The inner layer is modeled using a power-law velocity profile to represent the lower portion of the turbulent boundary layer, the same as used by Geller. Because the wake cannot be neglected in the elliptic problem, a simplifying assumption is required for its inner layer. The assumption is made that close to the wake centerline the vorticity varies linearly with radial distance. The presence of the inner layer results in a boundary condition of the third kind at the lower edge of the outer layer (the "patch boundary"). Once the solution in the inviscid, rotational domain is known, the pressure on the body and wake centerline is obtained by integrating the normal momentum equation downward from the patch boundary.

The reasons why the "frozen vorticity" approach can be highly automated and thus yield an easy-to-use computer code are (1) a considerable commonality exists in computational grids for the inviscid irrotational and rotational flowfields as well as the boundary layer, (2) the same body curve fit is used for all three flows, and (3) the starting profile for the inviscid rotational solution is generated automatically using computer-generated data files. The boundary-layer solution with viscid-inviscid interaction effects included takes only four steps: (1) a potential flow solution, (2) a corresponding boundary-layer solution, (3) a frozen vorticity solution, and (4) a final boundary-layer solution.

Equations of Motion

In cylindrical coordinates, (x, r, θ) where $\partial/\partial\theta = 0$ (axial symmetry) inviscid potential or rotational flow is governed by the equation

$$G_{xx} + G_{rr} - \frac{1}{r} G_r = -r^2 F(\psi) \quad , \quad (1)$$

where a lower case subscript denotes partial differentiation and G is the perturbation stream function defined by

$$G = \psi - \frac{1}{2} r^2 \quad . \quad (2)$$

The perturbation stream function is used because it is bounded as $r \rightarrow \infty$.

The reduced vorticity F is related to the vorticity ζ by

$$\zeta = rF(\psi) \quad . \quad (3)$$

The quantity F is uniquely determined by the upstream boundary condition.

For potential flow $F = 0$.

A body fitted coordinate system is introduced by the following general transformation:

$$x = x(\xi, \eta) \quad , \quad r = r(\xi, \eta) \quad , \quad (4)$$

where the coordinates (ξ, η) may or may not be orthogonal. Transforming to (ξ, η) coordinates, Eq. (1) becomes

$$G_{\eta\eta} - AG_{\eta} - 2BG_{\xi\eta} + CB_{\xi\xi} + DG_{\xi} = -E \quad , \quad (5)$$

where

$$A = \frac{1}{J_Y} [(J\beta)_\xi - (J_Y)_\eta + \frac{x_\xi}{r}] , \quad (6)$$

$$B = \frac{\beta}{Y} , \quad (7)$$

$$C = \frac{\alpha}{Y} , \quad (8)$$

$$D = \frac{1}{J_Y} [(J\alpha)_\xi - (J\beta)_\eta + \frac{x_\eta}{r}] , \quad (9)$$

$$E = \frac{r^2}{J^2_Y} F , \quad (10)$$

and

$$J = \text{Jacobian} = (x_\xi r_\eta - x_\eta r_\xi)^{-1} , \quad (11)$$

$$\alpha = x_\eta^2 + r_\eta^2 , \quad (12)$$

$$\beta = x_\xi x_\eta + r_\xi r_\eta , \quad (13)$$

$$\gamma = x_\xi^2 + r_\xi^2 . \quad (14)$$

Body Fitted Coordinates

A C-grid is the appropriate coordinate system in the present problem for proper flow resolution at the nose and downstream of the tail. A suitable C-grid, consisting of three regions, can be generated analytically, as illustrated in Fig. 1. The transformations are as follows:

(I) Orthogonal wrap-around grid, $0 \leq \xi \leq \xi_M$.

$$x = x_b(\xi) - \eta \sin \phi(\xi) \quad (15)$$

$$r = r_b(\xi) + \eta \cos \phi(\xi) \quad (16)$$

where x_b , r_b and ϕ as well as ξ and η are defined in Fig. 2.

(II) Sheared grid, $\xi_M \leq \xi \leq \xi_T$.

$$dx = \cos \phi(\xi) d\xi \quad (17)$$

$$r = r_b(\xi) + \eta \quad (18)$$

Note that for Regions I and II to be compatible, the junction must occur at the maximum body diameter.

(III) Cartesian grid, $\xi_T \leq \xi \leq \xi_R$.

$$x = \xi \quad (19)$$

$$r = \eta \quad (20)$$

The metric coefficients x_ξ , x_η , etc. are obtained analytically from Eqs. (15) through (20).

Potential Flow Boundary Conditions

For the potential flow case Dirichlet boundary conditions are specified on three sides of the computational domain (consisting of Regions I, II and III) and a Neumann condition on the fourth side. On the stagnation line (left boundary) $\psi = 0$ and hence

$$G(0, \eta) = 0, \quad 0 \leq \eta \leq \eta_U \quad (21)$$

Since the body and wake are part of the same streamline as the stagnation line, the condition $\psi = 0$ holds which leads to

$$G(\xi, 0) = \begin{cases} -\frac{1}{2} r_b^2, & 0 \leq \xi \leq \xi_T, \\ 0, & \xi_T \leq \xi \leq \xi_R. \end{cases} \quad (22a)$$

$$(22b)$$

At the outflow plane (right boundary) the flow is assumed to be uniform and parallel, the same as the free stream, and hence

$$G(\xi_R, \eta) = 0, \quad 0 \leq \eta \leq \eta_U. \quad (23)$$

Finally, the outer boundary is positioned far enough from the body so that the free-stream condition on velocity prevails, viz.

$$G_\eta(\xi, \eta_U) = 0, \quad 0 \leq \xi \leq \xi_R. \quad (24)$$

Equation (24) produces a better behaved numerical solution procedure than its Dirichlet counterpart $G(\xi, \eta_U) = 0$.

Frozen Vorticity Boundary Conditions

In the frozen vorticity case the computational domain consists of part of Region II and all of Region III with the lower boundary displaced upward a distance Δ from the body and wake centerline. The boundary condition on the upper boundary $\eta = \eta_U$ is the same as in the potential flow case. On the left or inflow boundary the stream function and vorticity are specified as a composite function of the potential flow and boundary-layer solutions, viz.

$$\left. \begin{aligned} G(\xi_{FV}, \eta) &= G_c(\eta) \\ F(\xi_{FV}, \eta) &= F_c(\eta) \end{aligned} \right\} , \quad 0 \leq \eta \leq \eta_U . \quad (25)$$

On the outflow plane (right boundary) parallel flow is assumed, as in the potential flow case. This assumption leads to

$$c_p(\xi_R, \eta) = 0 , \quad (26)$$

plus the following quadrature relation between r and ψ :

$$\psi = \frac{1}{2} \int_0^r dr^2 \quad \text{on } \xi_R , \quad 0 \leq \eta \leq \eta_U , \quad (27)$$

where from Bernoulli's equation and Eq. (26)

$$u = \sqrt{c_{p0}(\psi)} . \quad (28)$$

The numerical details of evaluating the inflow and outflow boundary conditions will be given later.

The boundary condition on the lower ("patch") boundary is obtained from considerations in the modeled turbulent boundary layer. The assumed "power law" velocity profile in this layer may be written as

$$u = u_\Delta \left(\frac{y}{\Delta} \right)^{\frac{1}{n}} , \quad (29)$$

where u_Δ is the axial velocity at $y = \Delta$ and is determined from the frozen vorticity solution. The stream function and axial velocity are related by

$$\psi_y = ru . \quad (30)$$

Integration of Eq. (30), using Eq. (29), between $y = 0$ and $y = \Delta$ yields

$$\psi_{\Delta} = U_{\Delta} \cdot \Delta \cdot \left(\frac{n}{1+n} r_b + \frac{n}{1+2n} \Delta \right) . \quad (31)$$

With the aid of Eqs. (2) and (30), u_{Δ} is found to be related to the n -derivative of G by

$$u_{\Delta} = 1 + \frac{(G_{\eta})_{\Delta}}{r_{\Delta}} . \quad (32)$$

The required boundary condition, upstream of the tail, is obtained by combining Eq. (2), evaluated at $y = \Delta$, with Eqs. (31) and (32). The result is

$$G_{\Delta} - \frac{K}{r_{\Delta}} (G_{\eta})_{\Delta} = K - \frac{1}{2} r_{\Delta}^2 , \quad \xi_{FV} \leq \xi \leq \xi_T , \quad (33)$$

where

$$K = \Delta \cdot \left(\frac{n}{1+n} r_b + \frac{n}{1+2n} \Delta \right) , \quad (34)$$

$$r_{\Delta} = r_b + \Delta . \quad (35)$$

In the wake the assumption is made that near $y = 0$ the vorticity is linear in y ,

$$\zeta = \zeta_{\Delta} \cdot \frac{y}{\Delta} . \quad (36)$$

Using Eq. (36) and neglecting $\partial v / \partial x$ (in keeping with the boundary-layer approximation), the vorticity definition can be integrated to yield the following expression for the centerline velocity:

$$u_C = u_{\Delta} + \frac{1}{2} \zeta_{\Delta} \cdot \Delta . \quad (37)$$

The integral of Eq. (2) between $y = 0$ and $y = \Delta$, making use of Eqs. (3) and (37), gives

$$\psi_{\Delta} = \frac{1}{2} u_{\Delta} \cdot \Delta^2 + \frac{1}{8} F(\psi) \cdot \Delta^4 . \quad (38)$$

When rewritten in terms of G_{Δ} and $(G_{\eta})_{\Delta}$ the wake boundary condition on $y = \Delta$ is obtained, viz.

$$G_{\Delta} - \frac{1}{2} \Delta \cdot (G_{\eta})_{\Delta} = \frac{1}{8} F(\psi) \cdot \Delta^4 , \quad \xi \geq \xi_T . \quad (39)$$

Numerical Algorithm

The main features of the numerical method used to solve the potential flow/frozen vorticity equation are as follows:

- (1) The transformed vorticity equation, Eq. (5), is written as a first-order system.
- (2) A fourth-order accurate spline, $S^1(4,0)$, is used in the η direction to resolve the vortical layer with as few nodal points as possible.
- (3) Second-order accurate finite difference formulas are used in the ξ -direction.
- (4) A nonuniform grid in η is generated by the use of a stretching function.
- (5) The resulting system of algebraic equations is solved by SLQR, sweeping in the ξ -direction.

To write Eq. (5) as a first-order system the following auxiliary variable is defined:

$$H = G_{\eta} \quad . \quad (40)$$

Then Eq. (5) may be written

$$H_{\eta} - AH - 2BH_{\xi} + CG_{\xi\xi} + DG_{\xi} = -E \quad . \quad (41)$$

The next step is the definition of the following spline first derivatives:

$$\varrho^G = G_{\eta} \quad , \quad (42)$$

$$\varrho^H = H_{\eta} \quad . \quad (43)$$

Then the governing equations, (40) and (41), become

$$\varrho^G - H = 0 \quad , \quad (44)$$

and

$$\varrho^H - AH - 2BH_{\xi} + CG_{\xi\xi} + DG_{\xi} + E = 0 \quad . \quad (45)$$

The finite difference expressions used for the ξ -derivatives are those given by Blottner [10] for a nonuniform grid, namely

$$(G_{\xi})_{i,j} = \frac{G_{i+1,j} - G_{i-1,j}}{\xi_{i+1} - \xi_{i-1}} \quad , \quad (46)$$

and

$$(G_{\xi\xi})_{i,j} = \frac{2}{\xi_{i+1} - \xi_{i-1}} \left[\frac{G_{i+1,j} - G_{i,j}}{\xi_{i+1} - \xi_i} - \frac{G_{i,j} - G_{i-1,j}}{\xi_i - \xi_{i-1}} \right], \quad (47)$$

plus an expression similar to Eq. (46) for $(H_{\xi})_{i,j}$. The ξ discretization of Eq. (45) leads to the following expression for unknowns at point (i,j) :

$$\ell_{i,j}^H - a_{i,j}G_{i,j} - b_{i,j}H_{i,j} = R_{i,j} \quad (48)$$

where

$$a_{i,j} = \frac{2}{\xi_{i+1} - \xi_{i-1}} \left(\frac{1}{\xi_{i+1} - \xi_i} + \frac{1}{\xi_i - \xi_{i-1}} \right) C_{i,j} \quad (49)$$

$$b_{i,j} = A_{i,j} \quad (50)$$

and

$$R_{i,j} = \frac{1}{\xi_{i+1} - \xi_{i-1}} \left[\left(\frac{2C_{i,j}}{\xi_i - \xi_{i-1}} - D_{i,j} \right) G_{i-1,j} + \left(\frac{2C_{i,j}}{\xi_{i+1} - \xi_i} + D_{i,j} \right) G_{i+1,j} \right] + \frac{2B_{i,j}}{\xi_{i+1} - \xi_{i-1}} (H_{i+1,j} - H_{i-1,j}) - E_{i,j} \quad (51)$$

The unknowns at node point (i,j) are G , ℓ^G , H and ℓ^H . Therefore, to complete the system two spline relations are needed. The governing equation has been written in first-order form so that the same spline relation, $S^i(4,0)$, can be used twice. The expression for $S^i(4,0)$ is (with i subscript understood) [11]

$$AA_j \phi_{j-1} + \sigma^2 \ell_{j-1}^\phi + BB_j \phi_j + (1 + \sigma)^2 \ell_j^\phi + CC_j \phi_{j+1} + \ell_{j+1}^\phi = 0, \quad (52)$$

where ϕ denotes G or H , and

$$AA_j = \frac{2\sigma^2(2 + \sigma)}{\Delta\eta_{j-1}(1 + \sigma)}, \quad (53)$$

$$BB_j = \frac{2(1 - \sigma)(1 + \sigma)^2}{\Delta\eta_{j-1}\sigma}, \quad (54)$$

$$CC_j = - \frac{2(1 + 2\sigma)}{\Delta\eta_{j-1}(1 + \sigma)\sigma}, \quad (55)$$

and

$$\sigma = \sigma_j = \frac{\Delta\eta_j}{\Delta\eta_{j-1}}, \quad (56)$$

$$\Delta\eta_j = \eta_{j+1} - \eta_j. \quad (57)$$

The number of unknowns at node point (i,j) is reduced from four to two by solving Eqs. (44) and (45) for $\ell_{i,j}^G$ and $\ell_{i,j}^H$, then substituting into the two tridiagonal spline relations. The resulting set may be written as the following tridiagonal matrix equation:

$$\hat{B}_{i,j}Z_{i,j-1} + \hat{A}_{i,j}Z_{i,j} + \hat{C}_{i,j}Z_{i,j+1} = \hat{D}_{i,j}, \quad 2 \leq j \leq N, \quad (58)$$

where the two-component column vector of unknowns $Z_{i,j}$ is defined by

$$Z_{i,j}^T = [G, H]_{i,j}. \quad (59)$$

The 2×2 matrix elements A , B and C and the two-component column vector D contain known quantities. These elements and components can be obtained from a combination of Eqs. (44), (45) and (52).

The boundary condition on the lower boundary ($\eta = 0$ or $\eta = \Delta$) can be written in the general form, valid for both potential and frozen vorticity cases,

where α and β are, except in one instance, functions of ξ . The exception is Eq. (39) where β depends on G .

The boundary conditions on the lower and upper boundaries together with a two point spline relation at each boundary close the system of equations at line i . The two-point spline relation used here is Eq. (16) of Reference 11, which in the present variables is

$$G_{i,2} - G_{i,1} - \frac{\Delta\eta_1}{2} H_{i,1} - \frac{\Delta\eta_1}{2} H_{i,2} + \frac{\Delta\eta_1^2}{12} \ell_{i,2}^H - \frac{\Delta\eta_1^2}{12} \ell_{i,1}^H = 0 \quad (61)$$

and

$$G_{i,N+1} - G_{i,N} - \frac{\Delta\eta_N}{2} H_{i,N} - \frac{\Delta\eta_N}{2} H_{i,N+1} + \frac{\Delta\eta_N^2}{12} \ell_{i,N+1}^H - \frac{\Delta\eta_N^2}{12} \ell_{i,N}^H = 0 \quad (62)$$

The above equations are fifth-order accurate in $\Delta\eta_j$ and have been found in the present application to maintain better overall solution accuracy than their lower-order cousins.

Upon elimination of ℓ^H using Eq. (45), the following matrix relations result at the boundaries:

$$\hat{A}_{i,1} Z_{i,1} + \hat{C}_{i,1} Z_{i,2} = \hat{D}_{i,1} \quad (63)$$

and

$$\hat{B}_{i,N+1} Z_{i,N} + \hat{A}_{i,N+1} Z_{i,N+1} = \hat{D}_{i,N+1} \quad (64)$$

For potential flow the singularity at the tail point and on the wake centerline requires special treatment. As can be seen, Eq. (5) at $r = 0$ reduces to $G_\eta = 0$. This condition, written as $H_{i,j} = 0$, replaces spline relation (61).

Along any line $i = \text{constant}$ the set of block tridiagonal equations

For potential flow the singularity at the tail point and on the wake centerline requires special treatment. As can be seen, Eq. (5) at $r = 0$ reduces to $G_\eta = 0$. This condition, written as $H_{i,j} = 0$, replaces spline relation (61).

Along any line $i = \text{constant}$ the set of block tridiagonal equations (58), (63) and (64) is solved by L-U decomposition using case (i) of Reference 12.

Map Junction Lines

For the coordinate system used in the present problem, the metric coefficients will be discontinuous at the junction of Regions I and II and the junction of Regions II and III. When a body has a series of curvature discontinuities, then Regions I and II are re-zoned with additional map junctions introduced at each curvature discontinuity. A "mapping region" is defined here to mean that portion of a map described by a coordinate transformation, Eq. (4), with continuous first and second derivatives.

At map junctions where the metric coefficients are discontinuous, Eq. (48) must be modified to account for such discontinuities. This process is performed using the generalized Chmielewski-Hoffman method of Reference 13. The author has found that ignoring these discontinuities leads to errors as large as 37 percent in the potential flow pressure coefficient.

In the C-H method, each adjoining domain is extended one step into the other to form a line of fictitious nodes. The equation of motion,

Eq. (5), is then written separately in the left and right regions at the junction. A condition of smoothness of derivatives of the solution must also exist across the junction. By combining the left and right forms of the governing equation with the smoothness condition, a single spline-finite-difference (SFD) equation is obtained at the junction line which accounts for the discontinuity in metric coefficients. For the algebraic details, the reader is referred to Reference 9.

Inflow and Outflow Conditions

For the frozen vorticity case the conditions on the inflow boundary are extremely important in determining the behavior of the solution near the body and wake centerline. Thus, care must be taken to determine these conditions accurately.

As already mentioned, these conditions are a composite of the potential flow and boundary-layer solutions at the initial line. This composite is calculated as follows:

- (1) The boundary-layer velocity and total head profiles for $\Delta \leq \eta \leq \eta_0$ are merged smoothly with their potential flow counterparts. For the velocity, smooth merging occurs in a natural manner. For the total head, the merging point is taken where c_{p0} in the boundary layer just becomes unity. As y increases, the total head in the boundary layer will exceed unity because the vertical component of velocity continues to increase.

(2) With u known on the inflow boundary (denoted by u_{FV}), the stream function is determined by numerical integration of

$$\frac{\partial \psi_{FV}}{\partial r} = (ru)_{FV} .$$

The integrations is carried out using the trapezoidal rule formula:

$$\psi_{FVj} = \psi_{FVj-1} + \frac{(\Delta \lambda_{FV})_{j-1}}{4} (u_{FVj-1} + u_{FVj}) , \quad (65)$$

where

$$\lambda = r^2 , \quad (66)$$

$$\Delta \lambda_j = \lambda_j - \lambda_{j-1} . \quad (67)$$

The perturbation stream function on the initial line is computed from Eq. (2).

(3) With $(c_{p0})_{FV}$ known, the reduced vorticity distribution, $F_{FV}(r)$, is determined from the relation:

$$F_{FV} = - \frac{1}{2ru} \frac{\partial (c_{p0})_{FV}}{\partial r} , \quad (68)$$

where the derivative of $(c_{p0})_{FV}$ with respect to r is calculated using a three-point unequally spaced finite difference formula.

The outflow stream function distribution ψ_R is also calculated using the trapezoidal rule, viz.

$$\psi_{Rj} = \psi_{Rj-1} + \frac{(\Delta \lambda_R)_{j-1}}{4} (u_{Rj-1} + u_{Rj}) , \quad (69)$$

where u_R depends on ψ_R through Eq. (28). Thus for each integration step, iteration is required to determine ψ_{Rj} during which u_{Rj} is allowed to lag one cycle. The foregoing procedure is much simpler and produces results almost as accurate as solving for ψ_R from a two-point boundary value problem using spline discretization.

Pressure on the Body Surface and Wake Centerline

For the frozen vorticity case the normal momentum equation, with viscous terms neglected, is used to determine the pressure on the body and wake centerline. Upon transformation to (ξ, η) coordinates and noting that in Regions II and III $x = x(\xi)$, this equation becomes

$$-\frac{\partial c_p}{\partial \eta} = 2\left(v - \frac{r_\xi}{x_\xi} u\right) \frac{\partial v}{\partial \eta} + 2 \frac{r_\eta}{x_\xi} u \frac{\partial v}{\partial \xi} \quad (70)$$

The finite difference form of Eq. (70) is obtained by centering at $\xi = \xi_i$ and $\eta = \Delta/2$ and approximating η -derivatives by central differences.

Then, applying the no-slip conditions at the wall and using eqs. (17) and (18) to determine the metric coefficients, the expression for the wall pressure is found to be

$$c_{p_{i,W}} = c_{p_{i,\Delta}} + \Delta c_{p_i} \quad (71)$$

where

$$\Delta c_{p_i} = (v - r'_b u)_{i,\Delta} v_{i,\Delta} + \frac{1}{2} u_{i,\Delta} \sqrt{1 + r'^2_{b_i}} (v_\xi)_{i,\Delta} \cdot \Delta$$

$$r'_b = \frac{dr_b}{dx} \quad (72)$$

The derivative of v with respect to ξ is computed by a second-order accurate three-point formula for unevenly spaced points. At the ends of the interval, second-order accurate one-sided formulas are used.

Results and Discussion

The main advantage of the frozen vorticity approximation over its competitors for solving the viscid-inviscid interaction problem is the high degree of automation possible. The key to automation is communication through automatically generated data files between the two computer codes that perform the various calculations. The two codes are:

- AXFL04 - This code performs potential flow-frozen vorticity calculations using the method given in this paper.
- BL20 - This code computes laminar/turbulent boundary layers using the Keller Box Method [14]. The algebraic turbulence model of Reference 15 is used.

The steps in a complete viscid-inviscid interaction calculation are as follows:

- (1) Using AXFL04 in the potential flow mode, a body pressure distribution is generated. Two data files are created, one for BL20 containing the pressure distribution and body curve fit, and the other for AXFL04 (frozen vorticity mode) containing the potential flow velocity profile at the initial value line.

- (2) BL20 is run next to obtain a boundary-layer solution using the potential flow pressure distribution from AXFL04 which contains the boundary-layer velocity profile at the initial value line. A double interpolation procedure is used to obtain values in cylindrical coordinates from those in boundary-layer coordinates.
- (3) AXFL04 is now run in the frozen vorticity mode to compute a modified body pressure distribution in the viscid-inviscid interaction region. The code automatically forms a composite initial value profile using data from steps 1 and 2. A data file is created for BL20 which contains the viscid-inviscid interaction body pressure distribution.
- (4) Using the pressure distribution from step 3, BL20 is re-run for the viscid-inviscid interaction body pressure distribution.

A nonuniform point distribution in η is generated using a one-sided Vinokur stretching function [16]. The stretching function of Vinokur was chosen because it produces a grid with a uniform truncation error independent of the governing equation or difference algorithm.

Although the same ξ -distribution is used in the potential and frozen vorticity calculations, the η distributions differ considerably. For proper resolution in the frozen vorticity case, about a third of the grid points must be placed in the thin vortical layer (the same thickness as the boundary layer). To do this requires a rapidly expanding grid in η since typically $\eta_0 \sim 2$. This is the main reason splines rather than finite differences were chosen to approximate flow derivatives in η .

An accurate body curve fit, a prerequisite in obtaining an accurate potential, boundary-layer and frozen vorticity solution, is achieved as

follows: With the body shape $r_b(x)$ given either analytically or discretely, the corresponding arc length distribution ξ is computed using the spline formula

$$\xi_i = \xi_{i-1} + \frac{h_i}{2} (u_{i-1} + u_i) - \frac{h_i^2}{12} (m_i - m_{i-1}) \quad , \quad (73)$$

where the two cases that must be considered are shown in the following table:

case	range	u	m	h
$x_b = x_b(r)$	$\left \frac{r'_b}{r_b} \right > 1$	$(1 + x'^2)^{1/2}$	$\frac{x'_b x''_b}{u}$	Δr_b
$r_b = r_b(x)$	$0 \leq \left \frac{r'_b}{r_b} \right < 1$	$(1 + r_b'^2)^{1/2}$	$\frac{r_b' r_b''}{u}$	Δx_b

Table 1. Body Arc Length Parameters

The first case, $x = x(r_b)$, is appropriate in the nose region of a blunt-nose body. The quantities x'_b , x''_b , r'_b and r''_b , required in the calculations, are computed in terms of arc length derivatives of these quantities which in turn are computed using a three-point uneven spacing formula.

Since m_i depends on ξ_i , Eq. (73) must be solved at each step by iteration. convergence is very rapid, usually requiring about four cycles. The use of Eq. (73) will produce a ξ distribution accurate to about four decimal places which assures that the derivatives required in the mapping are accurate and smooth. Test calculations have shown that Eq. (73) produces a ξ distribution three to four times more accurate than the chord formula in regions where r_b' is large and changing rapidly. In the process of determining ξ , the various mapping derivatives involving r_b will automatically be determined. For the boundary-layer solution, the derivative $du_e/d\xi$ is computed in the same way as body derivatives, using a three-point formula with unequal spacing.

The three bodies used as test cases in this paper are the same ones used in Reference 15, namely, the F-57 low-drag body of Parsons and Goodson [17], the modified spheroid of Patel [18] and the NSRDC streamlined body number 1 [19]. These bodies were chosen because of the high quality of the experimental data available for each.

The grid parameters used in the SFD solutions presented here are given in Tables 2 and 3 for potential flow and frozen vorticity cases respectively. Reynolds number for each test body (based on chord length) appears in Table 3. These Reynolds numbers correspond to values given in References 18-20.

	F-57	Spheroid	NSRDC No. 1
x_R	1.5	1.5	1.5
η_U	2.0	2.0	2.0
N_ξ	49	54	104
$(N_b)_\xi$	35	39	78
N_η	20	20	20
$\Delta\eta_1$	0.01119	0.01119	0.01119

Table 2. Potential Flow Solution Parameters.

	F-57	Spheroid	NSRDC No. 1
x_{FV}	0.707	0.681	0.687
x_R	1.5	1.5	1.5
n_U	2.0	2.0	2.0
N_ξ	32	31	51
$(N_b)_\xi$	14	16	25
N_η	40	40	40
$\Delta\eta_1$	0.00055	0.00055	0.00055
Δ	0.005	0.005	0.003
Re	1.2×10^6	1.262×10^6	6.6×10^6

Table 3. Frozen Vorticity Solution Parameters

The need for splines in the η -direction is clearly seen by contrasting values for $\Delta\eta_1$ in Tables 2 and 3. The frozen vorticity value is one twentieth as large as the potential flow value.

The number of grid points used for the NSRDC body is about twice that used for each of the others. The reason for this was to obtain adequate definition of the body pressure in the tail region where the NSRDC body has a double reflex.

Relaxation factors of 1.5 and 1.0 were used on G and H in all calculations. No optimization was attempted for these factors.

Convergence was considered accomplished in both potential and frozen vorticity runs when the absolute maximum change in H was less than 5×10^{-6} . The number of iterations required to reach convergence varied from 90 to 110 with typical CPU times on a VAX 11/780 computer ranging from two to three minutes. In all cases the maximum residual decreased smoothly as the number of iterations increased.

Boundary-layer solutions used the same ξ spacing as the potential flow calculations (as already mentioned). The number of points in the normal direction ranged from 30 at the nose to about 50 near the tail. To resolve the turbulent boundary layer properly, points were nonuniformly spaced using a geometric progression, with the smallest mesh at the wall. Typical CPU times were about 45 seconds. Thus, a complete viscid-inviscid solution cycle of four runs (potential flow, boundary layer, frozen vorticity and final boundary layer) took at most seven and a half minutes of CPU.

The frozen vorticity solution, having a truncated domain of dependence, will depend on the location of its initial value line, i.e., on the parameter x_{fv} . Experience has shown that at Reynolds numbers between 10^6 and 10^7 , (the range covered here) that the viscid-inviscid interaction region begins about 70 percent of the chord back from the nose. Thus a suitable choice for x_{fv} is about 0.7. Since the onset of the interaction region is gradual, the solution should not depend strongly on x_{fv} . To show that this is the case, different values of x_{fv} were tried for two of the three test bodies. The change in the maximum body pressure coefficient (which occurs near the tail) was taken as a measure of the sensitivity of the solution to changes in x_{fv} . For the

Modified Spheroid, a change in x_{FV} from 0.681 to 0.716 produced a change in maximum c_p of 1.9 percent while for the NSRDC body, a change in x_{FV} from 0.687 to 0.747 resulted in a change of 2.0 percent.

Since the solution is relatively insensitive to x_{FV} , the implication is that the reduced vorticity distribution on the initial value surface is essentially "frozen". This is indeed the case and is illustrated by Figure 3. The results in this figure are for the NSRDC body, but are typical for the other cases studied. The figure shows the variation of reduced vorticity F with stream function ψ for two choices of x_{FV} (0.687 and 0.747).

The "patching" of the inner and outer layers is responsible for introducing the parameter Δ into frozen vorticity solution. But what is Δ ? Is it merely a calibration parameter or does it correspond to some physical quantity in the turbulent boundary layer? To try to find the answer to this question, Δ was first assumed to be a calibration constant dependent only on Reynolds number. The calibration was performed using the F-57 body by requiring the predicted maximum body c_p to be the same as the experimental value. Using this procedure Δ was found to be 0.005. The same value was also used to compute the solution for the Modified Spheroid (since the Reynolds numbers are nearly the same). The value of Δ was reduced to 0.003 for the NSRDC body to account for the thinning of the boundary layer with increasing Reynolds number. At the initial value line the previously determined values of Δ in law-of-the-wall units varied from 200 to 750 whereas in terms of the boundary-layer thickness the range was from 0.15 to 0.20. When applied to the computed turbulent boundary layer at the initial plane, the calibrated values of Δ were

found not to correspond in any consistent manner to a meaningful length (such as the location of maximum Reynolds stress or the outer edge of the logarithmic region). Thus Δ seems merely to serve as a model calibration parameter.

As an indication of the sensitivity of the frozen vorticity solution to changes in Δ , several values were run for each body. Table 4 is a summary of the maximum pressure coefficient for these runs. The table shows that for two of the three test cases the solution is quite sensitive to variations in Δ . As Δ decreases maximum c_p is seen to increase with the percentage increase depending on the type of body. The Spheroid is by far the least sensitive.

Body	Δ	$c_{p_{\max}}$	x-Location
F-57	0.002	0.1986	0.889
F-57	0.003	0.1701	0.889
F-57	0.005	0.1613	0.889
Spheroid	0.002	0.2195	0.978
Spheroid	0.003	0.2184	0.978
Spheroid	0.005	0.2225	0.978
NSRDC	0.001	0.1793	0.968
NSRDC	0.003	0.1606	0.968

Table 4. Sensitivity of Computed $c_{p_{\max}}$ to Δ .

The computed body pressure distributions, both potential and frozen vorticity, are compared with experiment in Figures 4-6 for the F-57, Modified Spheroid and NSRDC bodies respectively. The values of Δ used are those given previously in this paper. In all cases the frozen vorticity pressure closely follows the experimental distribution. For the Spheroid the computed maximum c_p is too high. This is also the case in Reference 3 which uses the displacement body method (the present value is 0.223, Reference 3 gives 0.210 and experiment, from Reference 18 is 0.180).

Another item of interest in the present calculation scheme is the magnitude of the pressure change across the modeled turbulent layer. This change has been found to be quite small. In a typical run (the F-57 body with $\Delta = 0.003$) the increment, in terms of the surface pressure, reached a maximum of 1.8 percent very close to the tail.

The calculations of Geller [8], using a simplified frozen vorticity technique, show that the computed velocity profile (for the F-57 body) and the experimental profile develop almost identically with downstream distance. To check this observation, velocity profiles (frozen vorticity and turbulent boundary layer) were computed with the present procedure at several downstream stations. Since cylindrical coordinates are used in the comparison, a double interpolation procedure was necessary to obtain the boundary-layer profiles. The comparisons are shown for the F-57 in Figures 7-9 at three successive stations, $x = 0.844$, 0.933 and 0.978 . The frozen vorticity profile is seen to evolve differently from its

turbulent counterpart, becoming ever more concave as x increases. Apparently the poorer agreement with experiment in the present case is a result of the full elliptic problem being solved.

Concluding Remarks

A method for solving the axisymmetric viscid-inviscid interaction problem has been presented which predicts body pressure distributions with considerable accuracy and which is capable of a high degree of automation. In the method the flowfield is divided into an outer inviscid, rotational region where the vorticity is "frozen" and an inner viscous/turbulent region which is modeled by a power-law velocity profile. The solution to the frozen vorticity problem gives the viscid-inviscid interaction body pressure distribution which is then used as input to the standard axisymmetric turbulent boundary-layer equations. With this formulation, a complete solution to the viscid-inviscid interaction problem is obtained in four computation cycles. The method requires no user intervention between cycles and is more economical than solving the complete Navier-Stokes equations or the displacement body problem.

Results with the present method show that the outer rotational layer (frozen vorticity solution) controls the pressure in the viscid-inviscid interaction region near a body surface. This observation is in agreement with the findings of triple deck theory.

The present method is an approximate application of a triple deck in which the middle layer is ignored and, instead of asymptotic matching, the inner and outer layers are patched. The outer layer is solved in a

truncated computational domain with the initial value line positioned slightly upstream of the start of the interaction region. Thus, the outer solution depends on two geometric parameters, the patch distance and the axial location of the initial value line. Numerical tests have shown that the solution is relatively insensitive to the location of the initial value line but is affected significantly by the patch distance. Initial calculations indicate that the patch distance, which serves as a calibration parameter, depends only on Reynolds number. Once this parameter was determined, computed body pressure distributions in the viscid-inviscid interaction region (for three test bodies) were found to follow the experimental values very well.

Acknowledgement

The author is grateful to the Naval Sea Systems Command for their support of this work.

References

1. Huang, T. T., Wang, H. T., Santelli, N. and Groves, N. C., "Propeller/Stern/Boundary-Layer Interaction on Axisymmetric Bodies. Theory and Experiment," David W. Taylor Naval Ship Research and Development Center Report 76-0113, Bethesda, MD, December 1976.
2. Nakayama, A., Patel, V. C. and Landweber, L., "Flow Interaction Near the Tail of a Body of Revolution. Part II: Iterative Solution for Flow Within and Exterior to Boundary Layer and Wake," ASME Journal of Fluids Engineering, Vol. 98, Series 1, No. 3, 1976, pp. 538-549.
3. Hoffman, G. H., "A Modified Displacement-Body Method for Treating the Axisymmetric Strong-Interaction Problem," Journal of Ship Research, Vol. 24, No. 2, June 1980, pp. 114-122.
4. Carter, J. E., and Wornom, S. F., "Solutions for Incompressible Separated Boundary Layers Including Viscous-Inviscid Interaction," NASA SP-347, 1980.
5. Melnick, R. E., Chow, R. and Mead, H. R., "Theory of Viscous Transonic Flow Over Airfoils at High Reynolds Number," Paper No. 77-680, presented at AIAA 10th Fluid and Plasma Dynamics Conference, Albuquerque, NM, June 1977.
6. Melnick, R. E., and Grossman, B., "On the Turbulent Viscid-Inviscid Interaction at a Wedge-Shaped Trailing Edge," in Numerical and Physical Aspects of Aerodynamic Flows, T. Cebeci, ed., Springer Verlag, 1982, pp. 211-235.
7. Kuchemann, D., "Inviscid Shear Flow Near the Trailing Edge of an Airfoil," Z. Flugwiss., Heft 8/9, 1967, pp. 292-294.
8. Geller, E. W., "Calculation of Flow in the Tail Region of a Body of Revolution," Journal of Hydronautics, Vol. 13, No. 4, Oct. 1979, pp. 127-129.
9. Hoffman, G. H., "A Frozen Vorticity Approach to the Axisymmetric Strong Interaction Problem," ARL/PSU Technical Memorandum File No. TM 84-146, Applied Research Laboratory, The Pennsylvania State University, University Park, PA, 14 Sept. 1984.
10. Blottner, F. G., "Nonuniform Grid Method for Turbulent Boundary Layers," in Lecture Notes in Physics, Vol. 35, Springer-Verlag, 1975, pp. 91-97.
11. Rubin, S. G., and Khosla, P. K., "Polynomial Interpolation Methods for Viscous Flow Calculations," Journal of Computational Physics, Vol. 24, No. 3, July 1977, pp. 217-244.

12. Keller, H. B., "Accurate Difference Methods for Nonlinear Two-point Boundary Value Problems," SIAM Journal of Numerical Analysis, Vol. 11, No. 2, April 1974, pp. 305-320.
13. Chmielewski, G. E., and Hoffman, G. H., "Finite-Difference Solution of an Elliptic Partial Differential Equation with Discontinuous Coefficients," International Journal for Numerical Methods in Engineering, Vol. 12, 1978, pp. 1407-1413.
14. Cebeci, T., and Smith, A. M. O., "The CS Method" in Analysis of Turbulent Boundary Layers, Academic Press, New York, 1974, Chapter 7.
15. Hoffman, G. H., "An Algebraic Turbulence Model Modified for Extra Rates of Strain in an Axisymmetric Boundary Layer," ARL/PSU Technical Memorandum File No. TM 82-201, Applied Research Laboratory, The Pennsylvania State University, University Park, PA, 30 September 1982.
16. Vinokur, M., "On One-Dimensional Stretching Functions," Journal of Computational Physics, Vol. 50, 1983, pp. 215-269.
17. Parsons, J. S., and Goodson, R. E., "The Optimum Shaping of Axisymmetric Bodies for Minimum Drag in Incompressible Flow," Purdue University Report ACC-72-6, Lafayette, IN, June 1972.
18. Patel, V. C., Nakayama, A., and Damian, R., "Measurements in the Thick Axisymmetric Turbulent Boundary Layer Near the Tail of a Body of Revolution," Journal of Fluid Mechanics, Vol. 63, Part 2, 1974, pp. 345-367.
19. Huang, T. T., Santelli, N., and Belt, G., "Stern Boundary-Layer Flow on Axisymmetric Bodies," presented at Twelfth Symposium on Naval Hydrodynamics, Washington, DC 5-9 June 1978.
20. Patel, V. C., and Lee, Y. T., "Thick Axisymmetric Turbulent Boundary Layer and Near Wake on a Low-Drag Body of Revolution," Report No. 210, Iowa Institute of Hydraulic Research, Iowa City, IA, December 1977.

Nomenclature

c_p	static pressure coefficient
c_{p0}	total head
F	reduced vorticity - defined by Eq. (3)
G	perturbation stream function -- defined by Eq. (2)
H	derivative of G with respect to η - see Eq. (40)
ℓ^G	spline derivative approximation of $\frac{\partial G}{\partial \eta}$
ℓ^H	spline derivative approximation of $\frac{\partial H}{\partial \eta}$
N_ξ	number of nodes in the ξ -direction
$(N_b)_\xi$	number of ξ nodes on the body
N_η	number of nodes in the η -direction
r	radial coordinate
r_b	body radius
Re	Reynolds number, based on body length and free-stream speed
u	velocity component in x -direction
v	velocity component in r -direction
x	axial coordinate
ζ	vorticity magnitude
ξ	transformed coordinate along body and centerline
η	transformed coordinate away from body and centerline
ψ	stream function
ϕ	angle of tangent to body surface
θ	meridian angle

All other quantities are defined in the text.

Figure Captions

1. C-Grip Mapping.
2. Coordinates in Nose Region.
3. Reduced Vorticity Distribution on Initial Value Line, NSRDC Body.
4. Viscid-Inviscid Interaction Body Pressure Distribution, F-57 Body.
5. Viscid-Inviscid Interaction Body Pressure Distribution, Modified Spheroid.
6. Viscid-Inviscid Interaction Body Pressure Distribution, NSRDC Body No. 1.
7. Comparison of Turbulent Boundary-Layer and Frozen Vorticity Velocity Profiles at $x = 0.844$, F-57 Body.
8. Comparison of Turbulent Boundary-Layer and Frozen Vorticity Velocity Profiles at $x = 0.933$, F-57 Body.
9. Comparison of Turbulent Boundary-Layer and Frozen Vorticity Velocity Profiles at $x = 0.978$, F-57 Body.

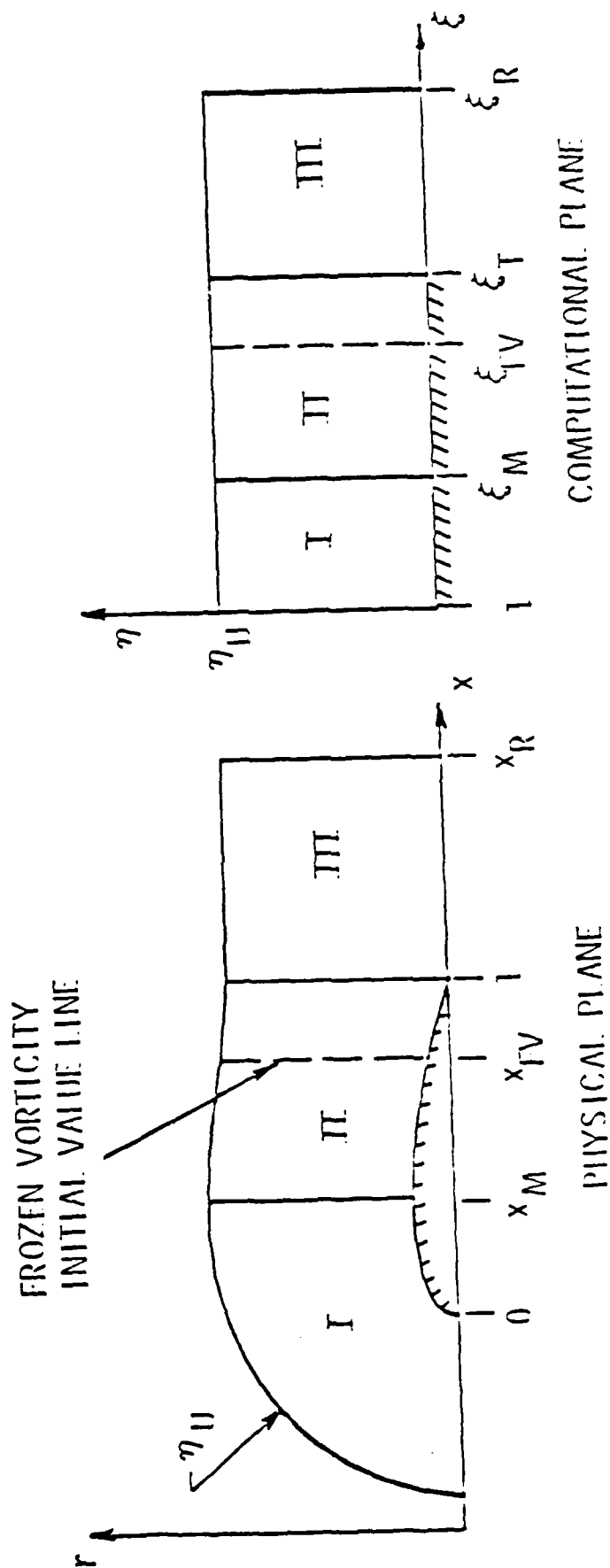


Figure 1. C-Grip Mapping.

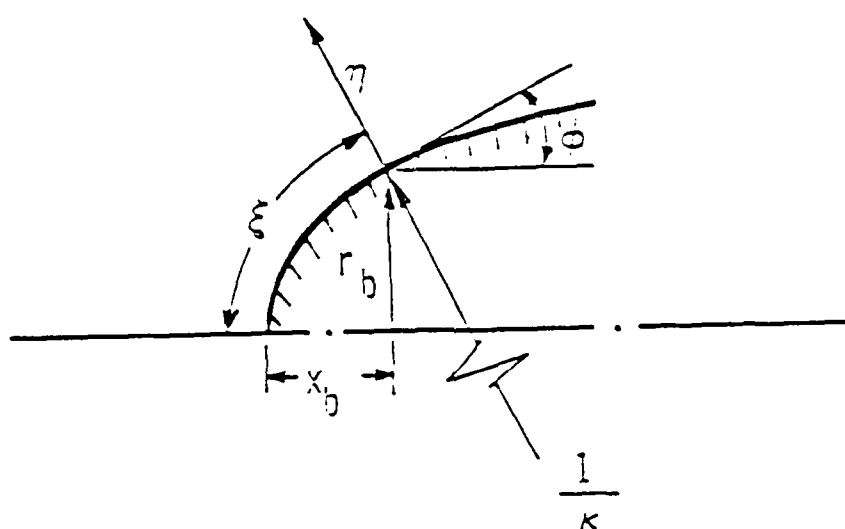


Figure 2. Coordinates in Nose Region.

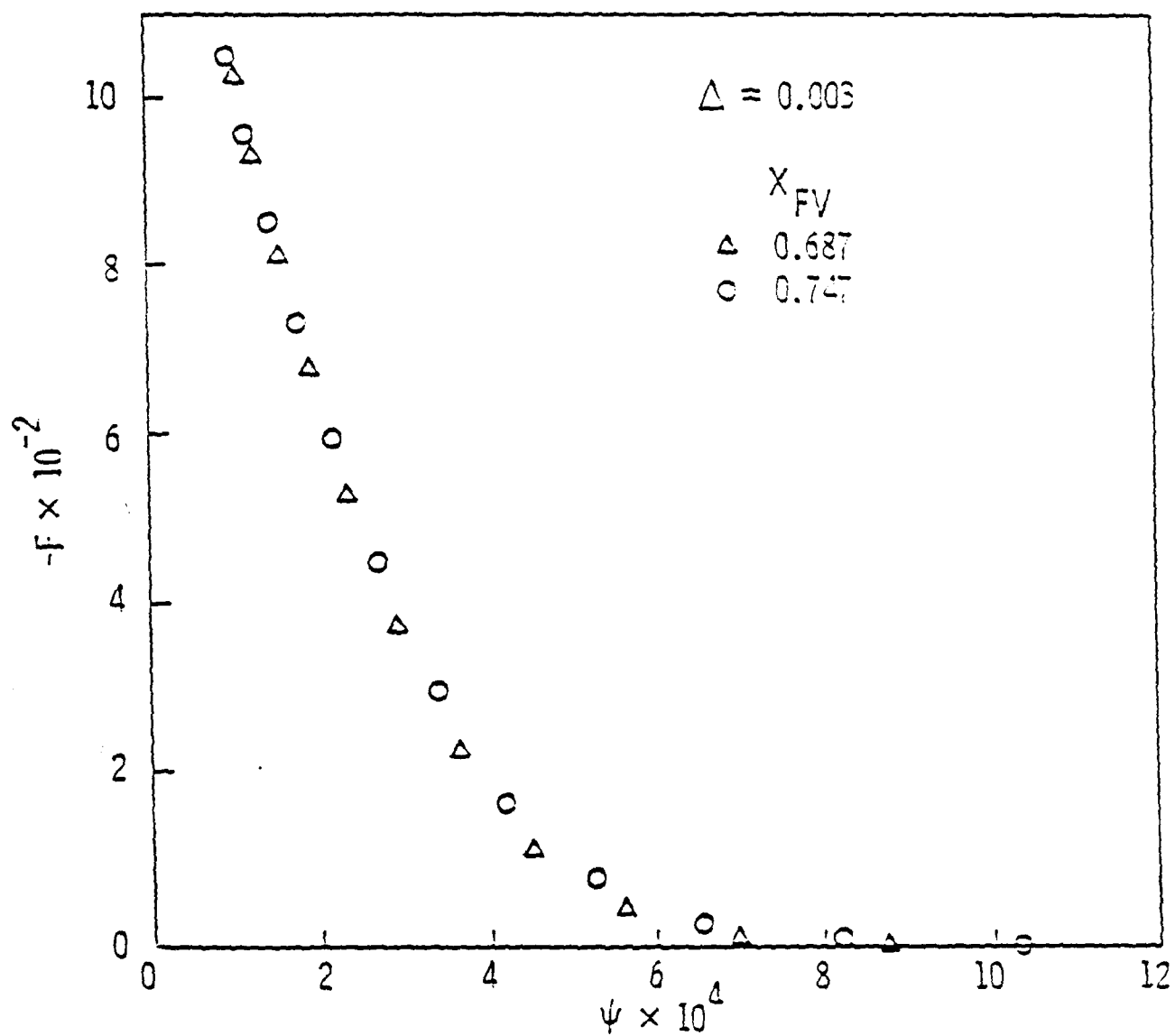


Figure 3. Reduced Vorticity Distribution on Initial Value Line, NSRDC Body.

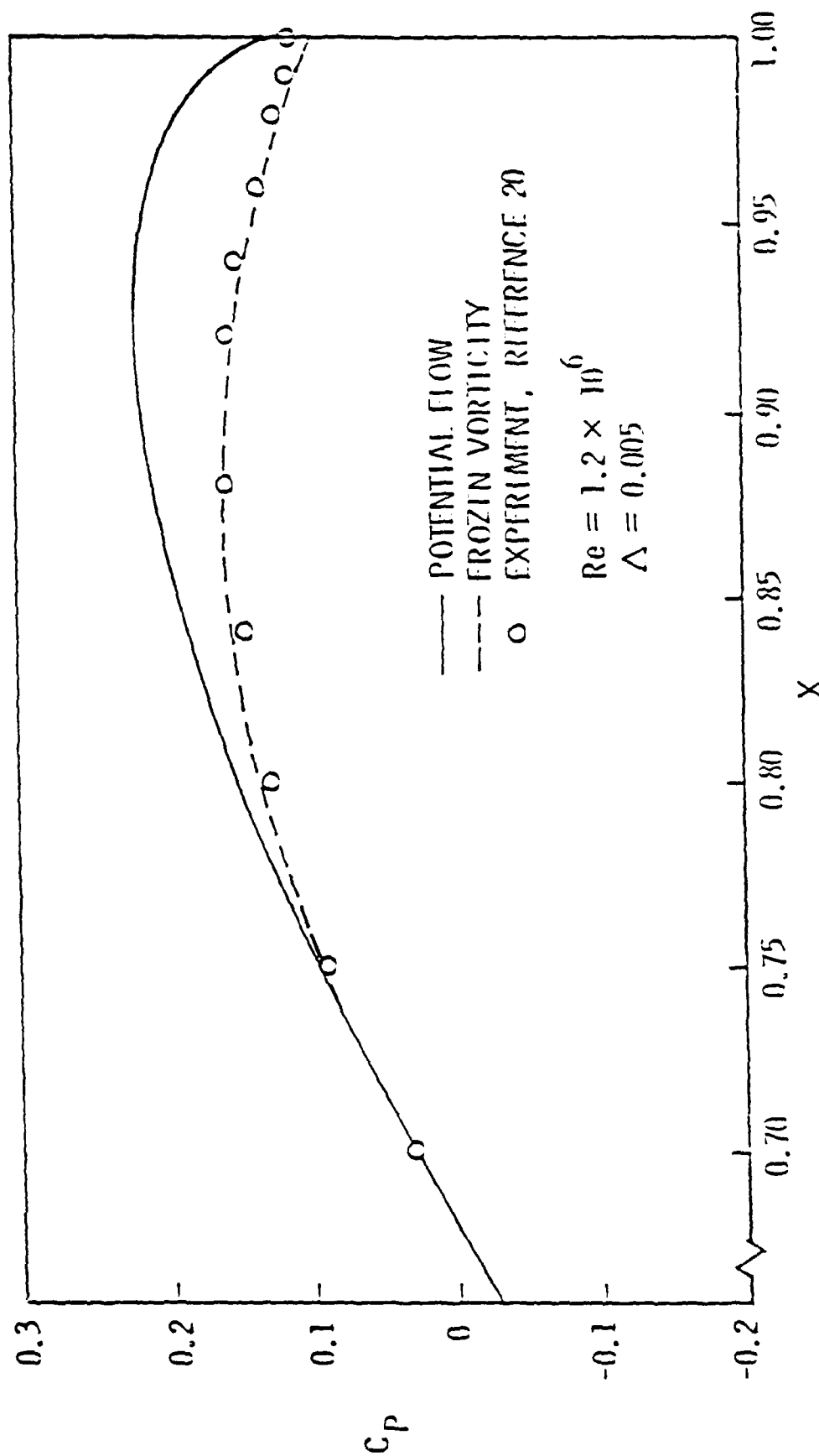


Figure 4. Viscid-Inviscid Interaction Body Pressure Distribution, F-57 Body.

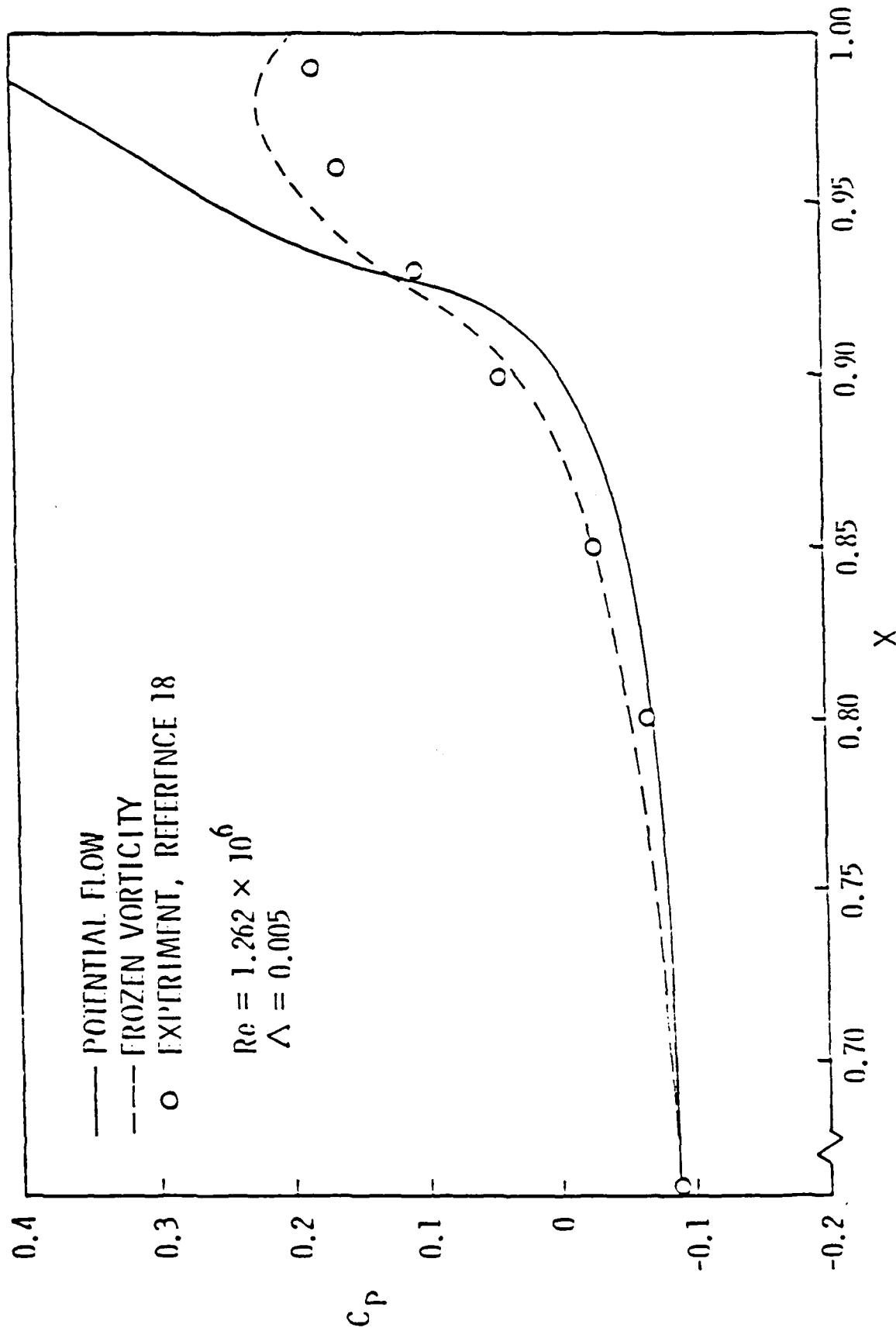


Figure 5. Viscid-Inviscid Interaction Body Pressure Distribution, Modified Spheroid.

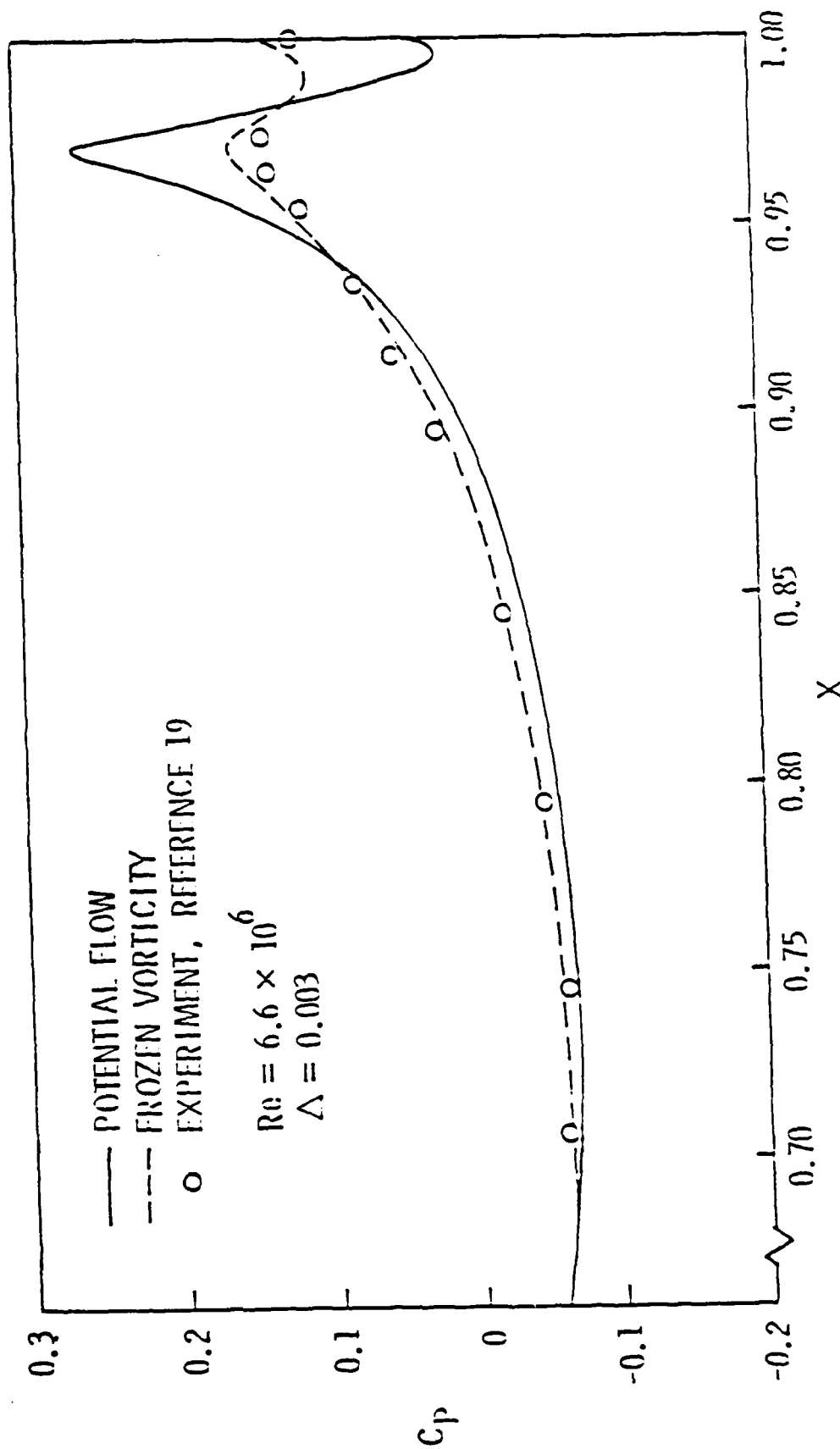


Figure 6. Viscid-Inviscid Interaction Body Pressure Distribution, NSRDC Body No. 1.

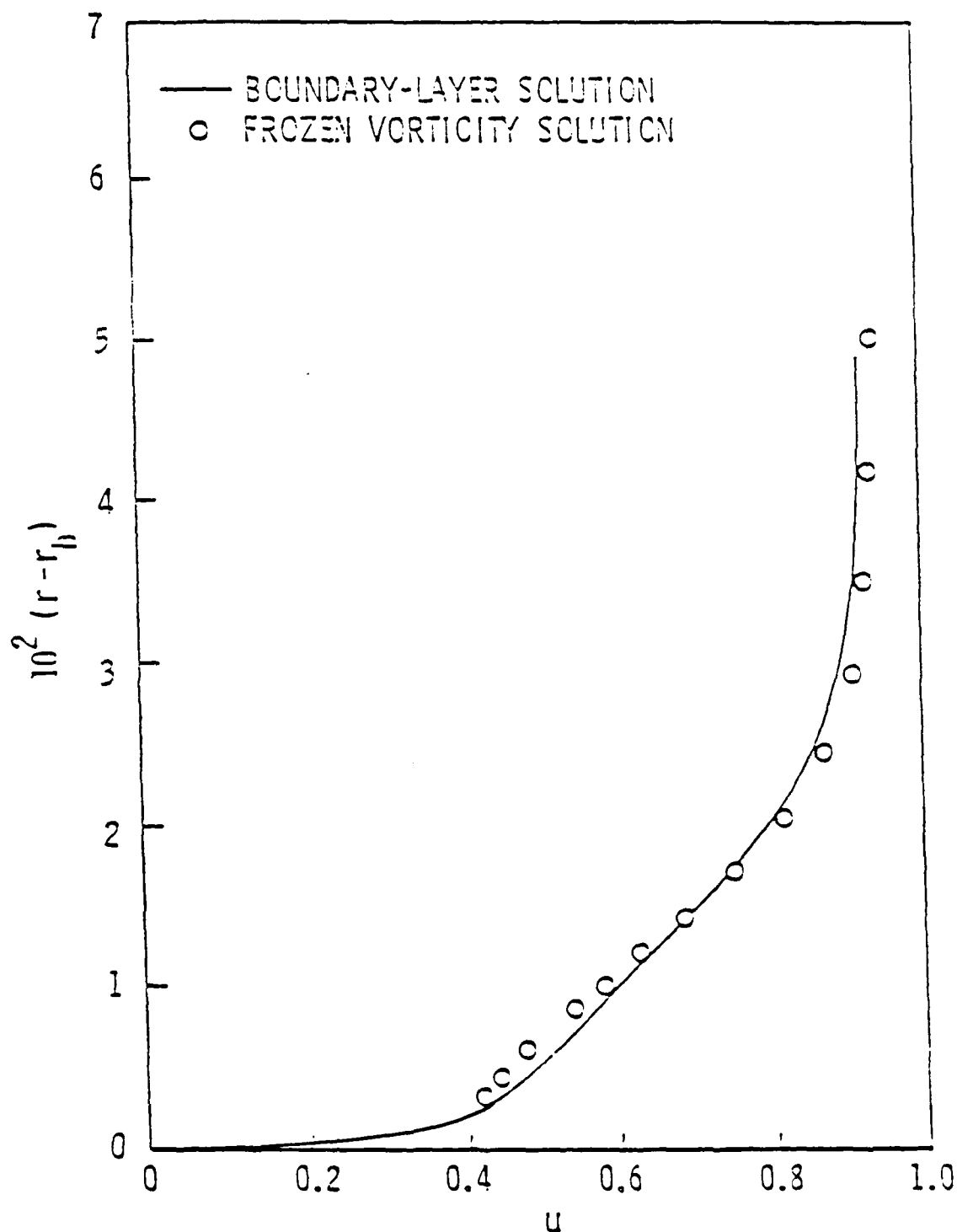


Figure 7. Comparison of Turbulent Boundary-Layer and Frozen Vorticity Velocity Profiles at $x = .844$, F-57 Body.

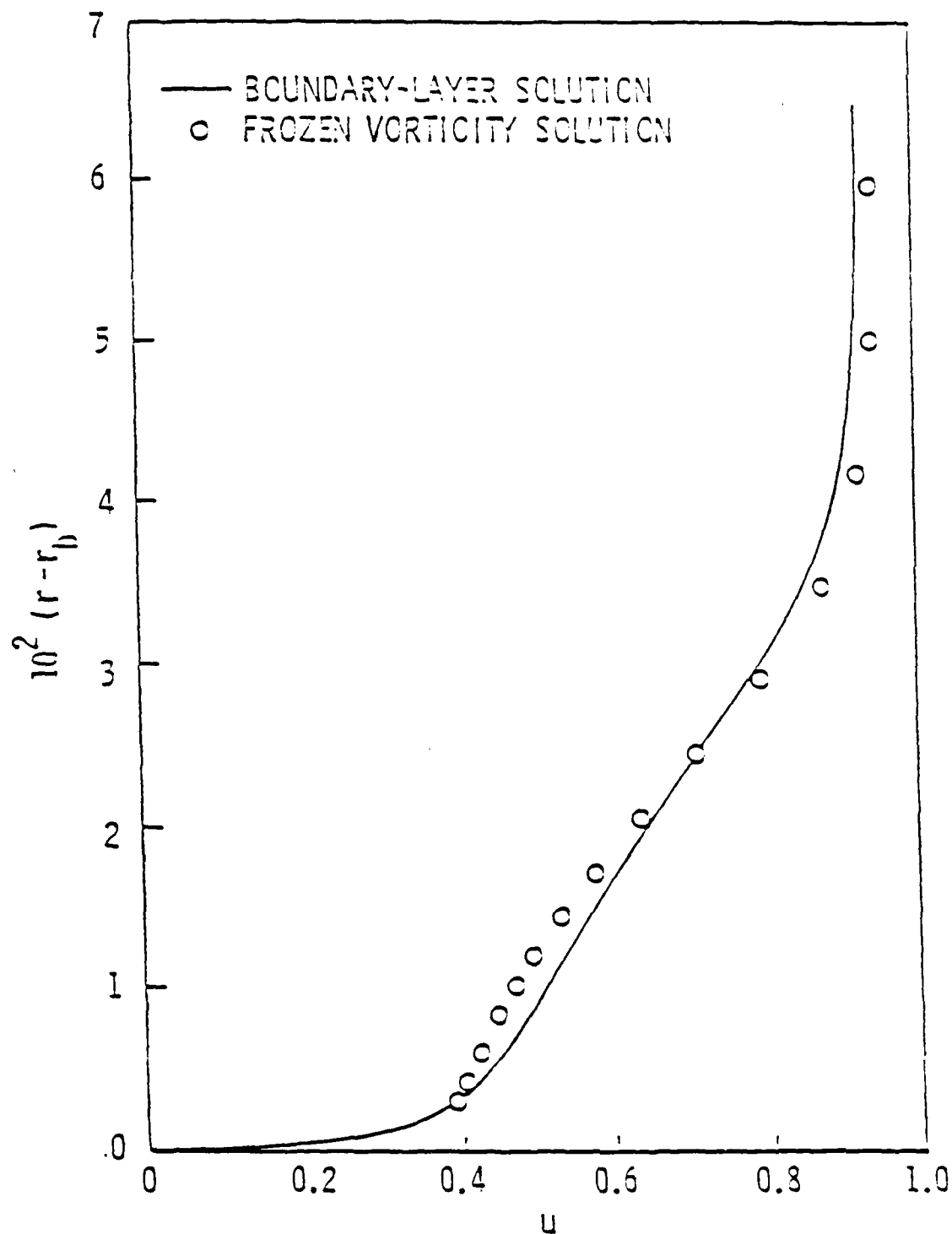


Figure 8. Comparison of Turbulent Boundary-Layer and Frozen Vorticity Profiles at $x = .933$, F-57 Body.

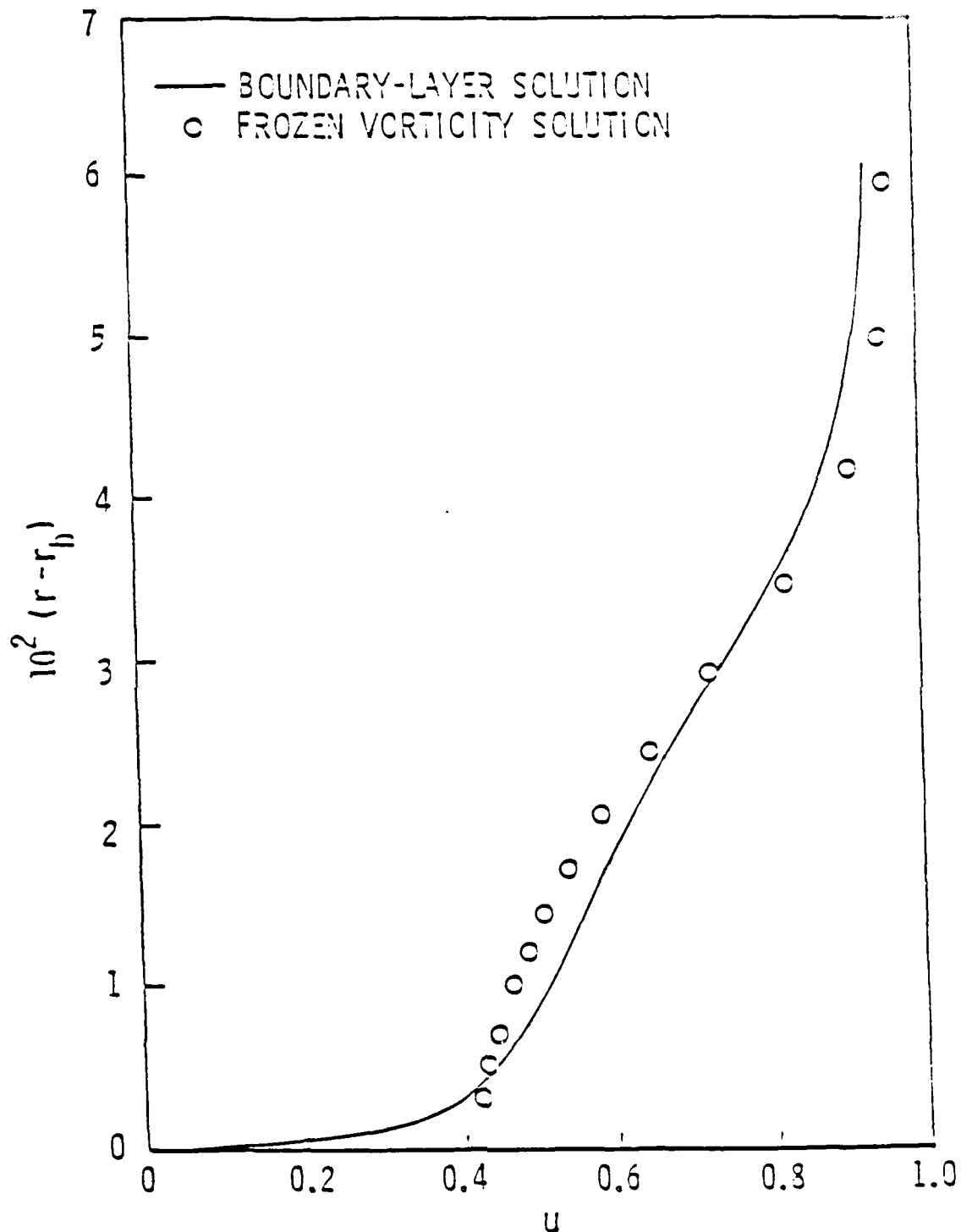


Figure 9. Comparison of Turbulent Boundary-Layer and Frozen Vorticity Velocity Profiles at 0.978, F-37 Body.

DISTRIBUTION LIST FOR UNCLASSIFIED ARL TM 88-12 by G. H. Hoffman, dated January 14, 1988.

Defense Technical Information
Center
5010 Duke Street
Cameron Station
Alexandria, VA 22314
(Copies 1 through 6)

Commander
David Taylor Research Center
Department of the Navy
Bethesda, MD 20084
Attn: T. T. Huang
Code 1552
(Copy No. 7)

David Taylor Research Center
Attn: Library
(Copy No. 8)

Commander
Naval Surface Weapons Center
Detachment
White Oak Laboratory
10901 New Hampshire Avenue
Silver Spring, MD 20903-5000
Attn: Library
(Copy No. 9)

Naval Research Laboratory
Department of the Navy
Washington, DC 20390
Attn: Library
(Copy No. 10)

Superintendent
Naval Post Graduate School
Monterey, CA 93949
Attn: Code 1424
(Copy No. 11)

Dr. James E. Carter
Manager, Computation Fluid
Mechanics Research
United Technologies Research
Center
East Hartford, CT 06108
(Copy No. 12)

Dr. R. E. Melnick
Director, Fluid Mechanics
Research & Development Ctr.
Grumman Aerospace Corp.
Bethpage, NY 11714
(Copy No. 13)

Dr. Joe F. Thompson
Dept. of Aerospace Engr.
Drawer A
Mississippi State University
Mississippi State, MS 39762
(Copy No. 14)

Commanding Officer
Naval Underwater Systems Center
Newport, RI 02840
Attn: D. Goodrich
Code 3634
(Copy No. 15)

Dr. C. L. Merkle
Dept. of Mechanical Engr.
The Pennsylvania State University
University Park, PA 16802
(Copy No. 16)

Applied Research Laboratory
The Pennsylvania State University
Post Office Box 30
State College, PA 1680
Attn: R. E. Henderson
(Copy No. 17)

Applied Research Laboratory
Attn: M. L. Billet
(Copy No. 18)

Applied Research Laboratory
Attn: T. A. Brungart
(Copy No. 19)

Applied Research Laboratory
Attn: K. J. Farrell
(Copy No. 20)

Applied Research Laboratory
Attn: M. W. McBride
(Copy No. 21)

Applied Research Laboratory
Attn: C. F. Smith
(Copy No. 22)

Applied Research Laboratory
Attn: GTWT Files
(Copy No. 23)

Applied Research Laboratory
Attn: ARL Library
(Copy No. 24)

END

DATE

FILMED

5-88

DTIC